ACS APPLIED MATERIALS & INTERFACES

Research Article

Cite This: ACS Appl. Mater. Interfaces 2017, 9, 36199-36205

www.acsami.org

Controlled Patterning of Plasmonic Dimers by Using an Ultrathin Nanoporous Alumina Membrane as a Shadow Mask

Qi Hao,[†,‡] Hao Huang,[‡,§] Xingce Fan,[§] Yin Yin,[†,∥] Jiawei Wang,[†] Wan Li,[‡] Teng Qiu,[§] Libo Ma,[*,†] Paul K. Chu,[*,‡] and Oliver G. Schmidt[†,∥]

[†]Institute for Integrative Nanosciences, Leibniz IFW Dresden, Helmholtzstraße 20, 01069 Dresden, Germany

[‡]Department of Physics and Materials Science, City University of Hong Kong, Tat Chee Avenue, Kowloon, Hong Kong 999077, China

[§]Department of Physics, Southeast University, Nanjing 211189, P. R. China

[∥]Material Systems for Nanoelectronics, Chemnitz University of Technology, Reichenhainer Str. 70, 09107 Chemnitz, Germany

Supporting Information

ABSTRACT: We report on design and fabrication of patterned plasmonic dimer arrays by using an ultrathin anodic aluminum oxide (AAO) membrane as a shadow mask. This strategy allows for controllable fabrication of plasmonic dimers where the location, size, and orientation of each particle in the dimer pairs can be independently tuned. Particularly, plasmonic dimers with ultrasmall nanogaps down to the sub-10 nm scale as well as a large dimer density up to 1.0×10^{10} cm^{-2} are fabricated over a centimeter-sized area. The plasmonic dimers exhibit significant surface-enhanced Raman scattering (SERS) enhancement with a polarization-dependent behavior, which is well interpreted by finite-difference time-domain (FDTD) simulations. Our results reveal a facile approach for controllable fabrication of large-area dimer arrays, which is of fundamental interest for plasmon-based applications in surface-enhanced spectroscopy, biochemical sensing, and optoelectronics.

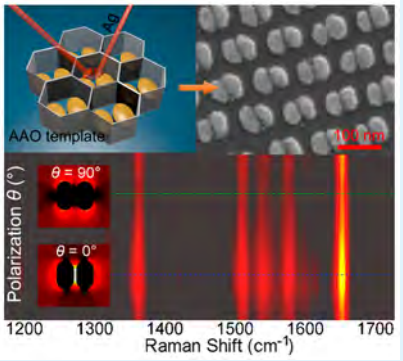

KEYWORDS: *dimer, nanofabrication, ultrathin anodic alumina membrane, shadow deposition, surface-enhanced Raman scattering*

INTRODUCTION

Plasmonic dimers consisting of pairs of coupled metallic nanoparticles have received increasing interest due to the ability to confine electromagnetic fields in their gaps.[1−3] Various fabrication techniques including bottom-up wet-chemistry growth[4,5] and top-down lithography[6−11] as well as characterization methods such as electron energy-loss spectroscopy[12−16] and dark-field scattering spectroscopy[17−21] have been adopted to investigate plasmonic coupling in the dimers by altering the dimer gap, particle size, or component materials. These investigations have spurred the application of plasmonic dimers to surface-enhanced Raman spectroscopy (SERS),[22−24] plasmon-enhanced photoluminescence,[25−28] nonlinear optical devices,[29,30] plasmon ruler,[31−34] and biochemical sensors.[35−39]

Implementation of dimers in practice requires repeatable, fast, and cost-efficient fabrication processes and the ability to efficiently optimize the dimer structure to cater to specific requirements. For instance, SERS which offers trace detection down to the single-molecule level[40−42] requires a sub-10 nm dimer gap and defined dimer orientation for efficient excitation by a polarized laser. Besides, a uniform pattern over a large area is crucial because the analytes are frequently randomly distributed on the substrate, but only molecules trapped in the gaps can provide dominant signals.[43] Among the current techniques to fabricate plasmonic dimers, top-down methods such as electron beam lithography (EBL) and focused ion beam (FIB) milling are time-consuming and costly especially for large area fabrication. With regard to the bottom-up method, dimers fabricated by wet-chemical methods tend to have irregular orientations and are prone to aggregation which can dramatically alter the plasmonic response.[44−46] In addition, a technique combining porous nanomasking and angle-resolved shadow deposition has exhibited the potential in fabricating complicated nanostructures.[47−50] However, facile production and optimization of the mask template for depositing dimers are still challenging.

Anodic aluminum oxide (AAO) is a popular nanotemplate due to the cost effectiveness and wafer-scale production.[51−54] The template can be transferred to the desired substrate as a nanomask to fabricate a myriad of nanostructures such as nanodots, nanowires, and nanoholes.[55−60] AAO possesses self-ordered and straight-through nanopores which are ideal for the preparation of dimers by angle-resolved shadow deposition. However, this strategy requires that the AAO membrane is ultrathin (<300 nm) and has the proper aspect ratio of film thickness to pore diameter, thereby making the preparation and

Received: August 1, 2017
Accepted: September 26, 2017
Published: September 26, 2017

DOI: 10.1021/acsami.7b11428
ACS Appl. Mater. Interfaces 2017, 9, 36199−36205

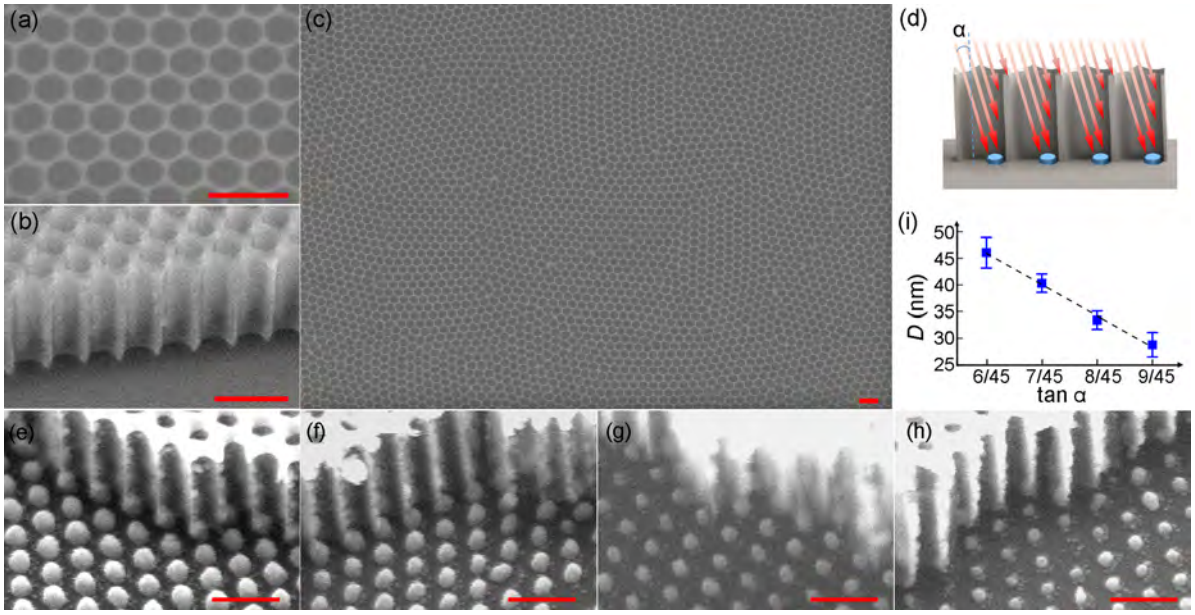

Figure 1. (a–c) Top-view, side-view, and large-area SEM images of the AAO membrane with a pore diameter of 80 nm, interpore distance of 100 nm, and film thickness of 250 nm. (d) Schematic of the angle-resolved shadow deposition method at a tilt angle α. (e–h) SEM images of the nanoparticle arrays for tan α = 6/45, 7/45, 8/45, and 9/45; (i) Variations in the nanoparticle size D as a function of tan α. The scale bars are 200 nm.

transfer procedures difficult. Herein, we overcome the limitation and demonstrate the use of the versatile AAO nanotemplate in the preparation of patterned dimer arrays with a tunable dimer size and controllable dimer gap down to the sub-10 nm scale. The dimer array exhibits defined dimer orientations and closely packed arrangements with a dimer density of up to 1.0×10^{10} cm^{-2} over a centimeter-sized area, thus providing an excellent platform for SERS detection and studying the corresponding polarization-dependent behavior. In addition, our approach provides sufficient degrees of freedom to design symmetrical/asymmetrical dimers with a rotatable orientation for each particle in the dimer pairs, consequently allowing flexible modulation of the plasmonic modes.

EXPERIMENTAL SECTION

Preparation of the Ultrathin AAO Membrane. The AAO membrane was formed on an aluminum foil (99.999%, 0.2 mm in thickness) by a typical anodization method. The aluminum foil was degreased with acetone, annealed at 400 °C for 30 min under vacuum to remove mechanical stress, and polished in a 1:4 solution of perchloric acid and ethanol at 15 V for 5 min. The first anodization step was performed in 0.3 M oxalic acid at 40 V and 0 °C for 12 h. The alumina formed in the first anodization process was dissolved by chemical wet etching in a solution of phosphoric acid (6 wt %) and chromic acid (1.8 wt %) with a volume ratio of 1:1 at 75 °C for 2 h. The aluminum foil was subjected a second anodization step the same as the first one for 10 min to produce the ultrathin AAO membrane. After the second anodization step, the AAO membrane was immersed in 5 wt % phosphoric acid at 30 °C for top etching to enlarge the AAO pores and then spin-coated with a PMMA layer at 600 rpm for 8 s and 3000 rpm for 60 s (Laurell spin coater WS-400BZ-6NPP-Lit). The remaining aluminum foil was etched in a 100 g L^{-1} $CuCl_2$ solution. Removal of the AAO barrier layer and bottom etching were carried out in a 5 wt % phosphoric acid solution to adjust the film thickness. Finally, the PMMA layer was dissolved in acetone, and the remaining AAO membrane was rinsed with distilled water several times and transferred onto the desired substrate. The top etching time was 23, 26, 29, and 35 min corresponding to bottom etching time of 24, 21, 18, and 12 min to obtain AAO with D = 70, 75, 80, and 90 nm, respectively. The film thickness of these AAO membranes was 250 nm and the differences in the etching procedures produced an error of less than 10 nm. More detailed information on how to fabricate and manipulate the ultrathin AAO membrane can be found from our previous publication.[60]

Angle-Resolved Shadow Deposition. The AAO membranes were placed on tilted substrates to perform angle-resolved shadow deposition. The E-beam deposition rate is 0.25 nm s^{-1}, and the deposition time is 100 and 120 s for the first deposition and the second one, respectively. AAO templates with pore diameters of 70, 75, and 80 nm were employed corresponding to deposition angles tan α = 7/45, 8/45 and 9/45 to fabricate homodimers with an estimated dimer gap of 8, 13, and 18 nm, respectively. The angled dimers were fabricated by placing the sample on a tilted substrate off the vertical center of the evaporation source.

Instrumentation and Data Acquisition. Field-emission scanning electron microscopy was performed on the JSM 7001F (JEOL), and the ImageJ software was used to conduct statistical analysis of the nanoparticle scale. The samples for SERS measurement were immersed in a 10^{-6} M solution of Rhodamine 6G in ethanol for 30 min, taken out, washed with copious amounts of ethanol, and dried under a stream of nitrogen. The Raman scattering spectra were collected on a Horiba confocal Raman spectrometer with a 457 nm laser line and a 50× objective. The SERS measurement was conducted at a low power (1.0×10^6 mW cm^{-2}) to prevent molecular photobleaching. The acquisition time was 30 s for SERS spectra and 5 s for SERS mapping. The Drude model was adopted in the FDTD method with a mesh size of 1 nm under plane wave excitation of 457 nm. The optical constants of Ag were taken from the literature.[61] The major axis and minor axis of the ellipsoidal particles were 60 and 30 nm, respectively.

RESULTS AND DISCUSSION

The AAO nanotemplate is anodized on an aluminum foil and transferred to a silicon substrate as a shadow nanomask to perform angle-resolved shadow deposition. Specific information on the preparation procedures can be found in the Experimental Section. Figure 1a–c display the scanning electron microscopy (SEM) images of AAO membrane with a hexagonally close-packed nanopore structure. The pore diameter is variable from 15 to 400 nm and interpore spacing

DOI: 10.1021/acsami.7b11428
ACS Appl. Mater. Interfaces 2017, 9, 36199–36205

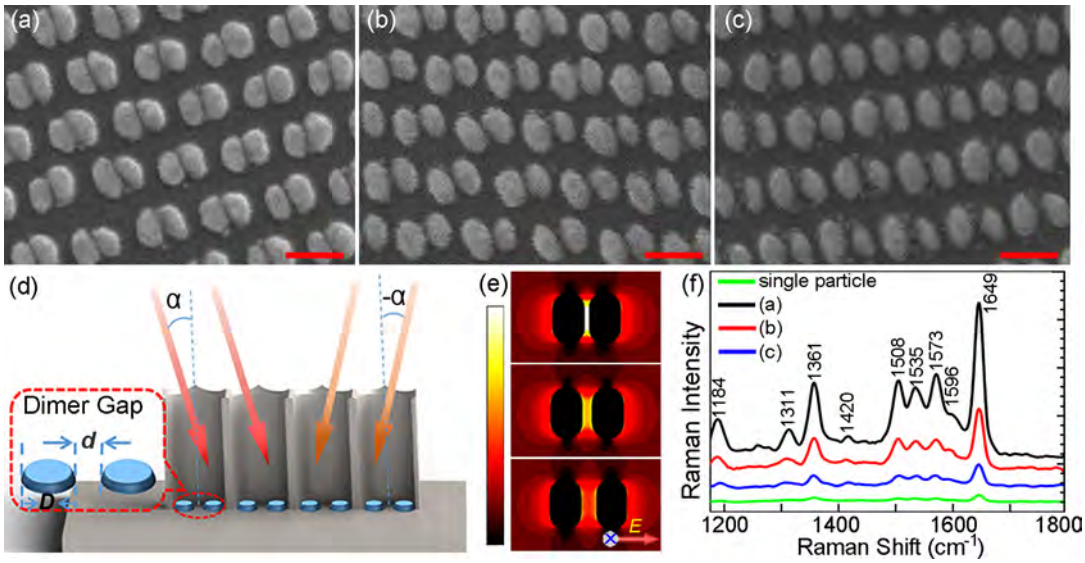

Figure 2. (a–c) SEM images of the silver dimers with different dimer gaps of d = 8 , 13, and 18 nm, respectively, and scale bars being 100 nm. (d) Schematic showing the preparation of plasmonic homodimers in angle-resolved shadow deposition. (e) Calculated electric fields around the plasmonic dimers when excited by the 457 nm laser with the dimer long axis parallel to the incident polarization E. (f) Raman scattering spectra of Rhodamine 6G molecules acquired from the plasmonic dimer arrays shown in (a–c) and on a single silver nanoparticle array.

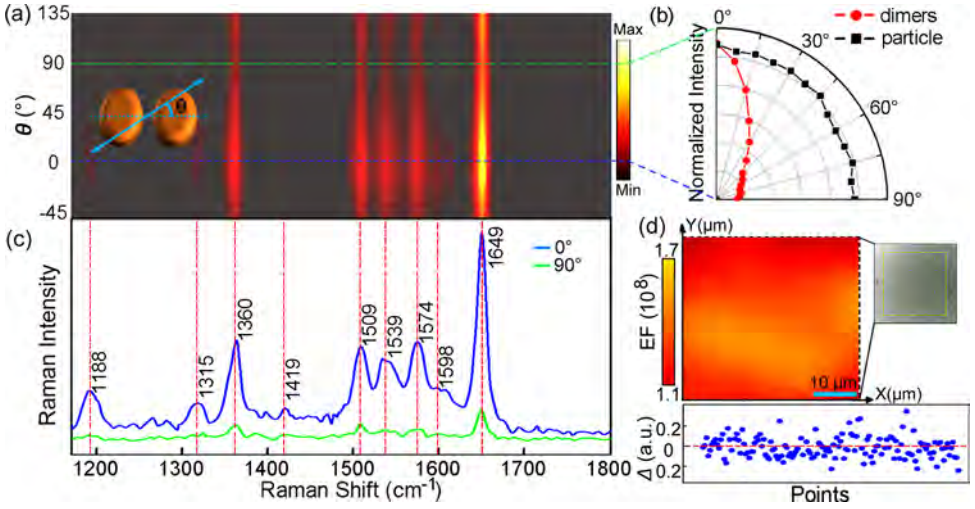

Figure 3. SERS of Rhodamine 6G molecule measured from the plasmonic dimer array (d = 8 nm). (a) SERS map as a function of θ, which represents the angle of excitation laser polarization with respect to the dimer orientation with laser polarization represented by the arrow in the inset. (b) Normalized Raman intensity from the dimer array and single silver nanoparticle array as a function of laser polarization angles by analyzing the integral Raman intensity of the 1649 cm^{-1} band. (c) SERS spectra taken with the laser polarization being parallel (θ = 0°) and perpendicular (θ = 90°) to the dimer long axis. (d) SERS map (44 μm × 44 μm) of the silver dimer array obtained from the integrated intensity of the 1649 cm^{-1} band by measuring 144 points with a scanning step of 4 μm. The detection area for the SERS map is shown in the optical photo, and the relative error (Δ) of each point is plotted in the bottom panel.

is tunable from 50 to 400 nm by adjusting the anodization conditions.[62,63] The AAO membranes are placed on tilted substrates to adjust the deposition angle α for angle-resolved shadow deposition, as illustrated in Figure 1d. Figure 1e–h show the series of nanoparticle arrays deposited at different deposition angles α. The deposited nanoparticles have an ellipsoidal shape with size (D) along the minor axis of the deposited nanoparticle varying with α. The particle size D changes from 46 nm, to 42, 35, and 31 nm when depositing at tan α = 6/45, 7/45, 8/45, and 9/45, respectively (also see Figure S1 and Table S1). The particle density is calculated to be 1.0 × 10^{10} cm^{-2} according to the SEM images. The results show that D can be continuously controlled by adjusting the deposition angle, and it is thus a convenient approach to tune the particle size and subsequent dimer gap.

The dimer arrays are fabricated by evaporating plasmonic materials from two opposite angles through the AAO pores onto the substrate, as shown in Figure 2. Figure 2a–c display the ellipsoidal homodimers with different dimer gaps d. The dimer arrays with dimer gaps of 8, 13, and 18 nm are fabricated to demonstrate that d can be continuously varied down to the sub-10 nm regime, which is close to the resolution of lithographic techniques. The AAO with different pore diameters of 70, 75, and 80 nm are employed corresponding to deposition angles tan α = 7/45, 8/45, and 9/45, respectively, to maintain the particle size while adjusting the dimer gap.

DOI: 10.1021/acsami.7b11428
ACS Appl. Mater. Interfaces 2017, 9, 36199–36205

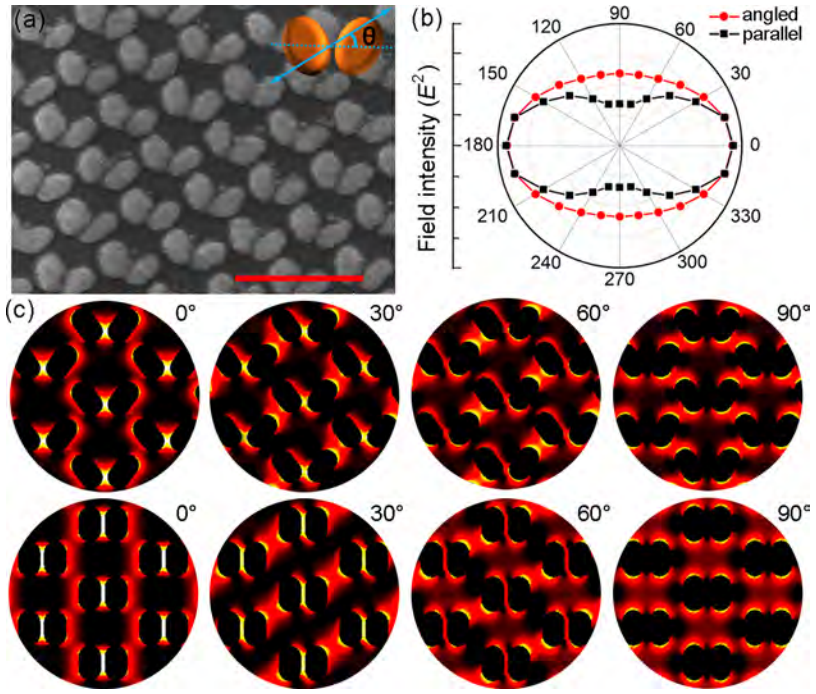

Figure 4. (a) SEM image of the angled ellipsoidal dimers with the intersection angle between two ellipsoidal particles in pairs being 60° and scale bar being 200 nm. (b) Variations in the calculated electric field density ($|E|^2$) of the angled dimers and paralleled dimers in relation with the laser polarization angle θ. (c) Calculated electric field distribution of the angled dimers and paralleled dimers under different excitation polarizations.

Finite-difference time-domain (FDTD) simulation is performed to evaluate the efficiency of the plasmonic dimers, as shown in Figure 2e. The calculated electric field distribution shows that strongly enhanced fields, so-called "hot spots", are observed between the nanoparticle pairs. As the interparticle distance decreases, the interaction between the nanoparticles strengthens, resulting in enhanced electric field in the gap region and yielding high-sensitivity SERS detection. The SERS spectra of Rhodamine 6G molecules acquired from the plasmonic dimers with different gaps are presented in Figure 2f. The results reveal that the Raman signal on the dimer array with d = 8 nm is enhanced by ~40 times compared to a single silver particle nanoarray fabricated similarly but without a second shadow deposition process. Moreover, our strategy enables the fabrication of plasmonic dimers with different particle sizes while keeping the gap distance constant (see Figure S2).

Figure 3 shows the SERS spectra of Rhodamine 6G molecules acquired from the plasmonic dimers with d = 8 nm. The polarization Raman map in Figure 3a exhibits that the SERS signal varies as a function of the laser polarization angle θ. This polarization-dependent variation can be clearly observed from the corresponding polar-diagram in Figure 3b. Figure 3c displays the representative SERS spectra with the laser polarization being parallel (θ = 0°) and perpendicular (θ = 90°) to the dimer long axis. Owing to the confined electric field, some Raman peaks (e.g., at 1188, 1315, 1419 nm) are resolved at 0° but disappear when laser polarization does not match the dimer long axis. The integral Raman intensity at θ = 0° is improved by approximately 9 times than intensity at θ = 90°, demonstrating the dependence of laser polarization in the SERS measurement. This polarization-dependent enhancement is not observed from a single silver particle array indicating that localized surface plasmon resonance (LSPR) confined in the dimer gap is responsible for this phenomenon. The homogeneity of the silver dimer array is evaluated by 2D point-by-point SERS mapping as shown in Figure 3d which reveals excellent uniformity over a large area. The relative SERS peak intensity of the spots is centered in a narrow range with a standard deviation of 0.13 and average EF of 1.4×10^8 times based on the classical calculation expression[23] (also see Supporting Information). It should be noted that the surface roughness and the small dots around the dimer particles may have a perturbation effect on the plasmon resonances. For simplicity, this perturbation was neglected in the calculation. In addition, the large-area SEM image consisting of more than 10 000 plasmonic dimers also verifies the sample homogeneity (Figure S2).

The technique described here allows custom design of plasmonic dimers with a variable intersection angle. Figure 4a shows the angled silver dimers fabricated by off-center deposition along the AAO pores. In the angled dimer array, LSPR can form at different intergaps (e.g., within a dimer, or between dimers) depending on the excitation polarization. The calculated electric field density ($|E|^2$) of the paralleled dimers and angled dimers as a function of the polarization angles is plotted in Figure 4b and the corresponding electric field distributions are displayed in Figure 4c. Compared to the paralleled dimers, some favorable LSPR modes are observed between neighboring dimers when the excitation polarization is tuned away from the dimer long axis (e.g., at 30°). This characteristic can potentially provide tunable and switchable LSPR modes formed at different gap sites for specific plasmonic applications. It is known that control over the gap distance can efficiently tune the plasmonic resonance modes, but it is undesirable because the increase in the dimer gap is always accompanied by a sacrifice in the electric field enhancement. Here, our angled elliptical dimers provide the possibility to modulate plasmonic resonance modes by altering the contacting angles and/or changing the excitation polarization.

DOI: 10.1021/acsami.7b11428
ACS Appl. Mater. Interfaces 2017, 9, 36199−36205

As mentioned above, the gaps between particles are crucial to LSPR-based applications. In addition to manipulating the dimer gap in each individual AAO pore, we can adjust the interspacing between the dimer pairs by varying the separation between AAO pores, thus enabling further modulation of LSPR. In this way, the AAO walls are used as a separation between the deposited nanoparticle and the gaps formed when AAO is peeled off. The SEM image in Figure 5 displays the fabricated

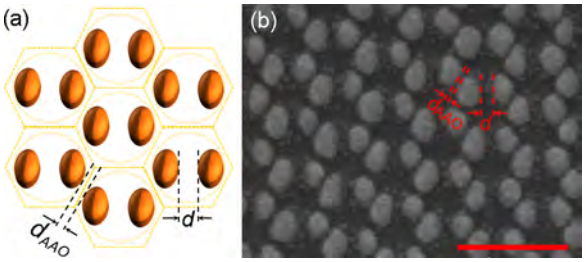

Figure 5. (a) Schematic and (b) corresponding SEM image of the hexagonal "flower" patterns fabricated by controlling the interspacing between AAO pores d_{AAO}, with the scale bar being 200 nm.

hexagonal "flower" patterns by adopting an AAO membrane with an interpore distance d_{AAO} of 10 nm. The results demonstrate that d and d_{AAO} can be individually controlled to optimize the LSPR from the dimer patterns. In fact, this configuration can also be used to design dimers with d_{AAO}, but not d, as the dimer gap. In this way, dimers with a fixed gap can be obtained despite the deposition angles at the same time, and consequently, undesired formation of bridges between dimers can be avoided. However, the minimum value of d_{AAO} is about 10 nm because smaller wall thickness makes it difficult to handle the ultrathin AAO membrane.

In addition to homodimers, which have the same particle size and component material, our strategy can be extended to fabricate asymmetrical heterodimers with a tunable particle size ratio (see Figure S3) compatible with multiple compositions (e.g., silver/gold dimers). The mismatch in size or material is particularly interesting for the excitation of higher order plasmon modes, in which the symmetry breaking allows for both far-field and near-field excitation/probing. Moreover, a rich set of properties that cannot be easily observed in homodimers such as the plasmonic dark modes[64] and plasmon-induced Fano profiles[65−67] can be expected from the asymmetrical dimers.

CONCLUSIONS

We demonstrate the tunable and controllable fabrication of plasmonic dimer arrays by utilizing an ultrathin AAO membrane as a mask template for angle-resolved shadow deposition. Plasmonic dimer arrays with a defined orientation, controllable particle size, and tunable gap distance over a large area are fabricated and characterized. The plasmonic dimer array with sub-10 nm dimer gaps exhibits significant SERS enhancement. In addition, polarization-dependent SERS enhancement is revealed depending on the dimer orientation and laser polarization. Moreover, our approach also enables flexible tuning of the intersection angle of plasmonic dimers as well as interspacing of the dimers, consequently allowing for high degree-of-freedom manipulation of LSPR from the dimer arrays.

ASSOCIATED CONTENT

Supporting Information

The Supporting Information is available free of charge on the ACS Publications website at DOI: 10.1021/acsami.7b11428.

Additional description and experimental data on the optimization of angle-resolved shadow deposition, manipulation of deposited particle size, and fabrication of homodimers with tunable particle scale and heterodimers with different particle size ratio (PDF)

AUTHOR INFORMATION

Corresponding Authors

*E-mail: l.ma@ifw-dresden.de (L. M.).
*E-mail: paul.chu@cityu.edu.hk (P. K. C.).

ORCID

Qi Hao: 0000-0002-5525-4417
Yin Yin: 0000-0002-5318-0020
Teng Qiu: 0000-0002-1160-2619
Libo Ma: 0000-0001-9850-2292

Author Contributions

The manuscript was written with contributions from all authors. All authors have given approval to the final version of the manuscript.

Notes

The authors declare no competing financial interest.

ACKNOWLEDGMENTS

This work was supported by German Research Foundation (DFG) No. 1713. P.K.C. acknowledges City University of Hong Kong Applied Research Grant (ARG) No. 9667122 as well as the Hong Kong Research Grants Council (RGC) General Research Funds (GRF) No. CityU 11301215.

REFERENCES

(1) Nordlander, P.; Oubre, C.; Prodan, E.; Li, K.; Stockman, M. I. Plasmon Hybridizaton in Nanoparticle Dimers. *Nano Lett.* **2004**, *4*, 899−903.

(2) Halas, N. J.; Lal, S.; Chang, W.-S.; Link, S.; Nordlander, P. Plasmons in Strongly Coupled Metallic Nanostructures. *Chem. Rev.* **2011**, *111*, 3913−3961.

(3) Zhu, W. Q.; Esteban, R.; Borisov, A. G.; Baumberg, J. J.; Nordlander, P.; Lezec, H. J.; Aizpurua, J.; Crozier, K. B. Quantum Mechanical Effects in Plasmonic Structures with Subnanometre Gaps. *Nat. Commun.* **2016**, *7*, 11495.

(4) Sardar, R.; Heap, T. B.; Shumaker-Parry, J. S. Versatile Solid Phase Synthesis of Gold Nanoparticle Dimers Using an Asymmetric Functionalization Approach. *J. Am. Chem. Soc.* **2007**, *129*, 5356−5357.

(5) Fang, L. L.; Wang, Y. L.; Liu, M.; Gong, M.; Xu, A.; Deng, Z. X. Dry Sintering Meets Wet Silver-Ion "Soldering": Charge-Transfer Plasmon Engineering of Solution-Assembled Gold Nanodimers from Visible to near-Infrared I and Ii Regions. *Angew. Chem., Int. Ed.* **2016**, *55*, 14296−14300.

(6) Schuck, P.; Fromm, D.; Sundaramurthy, A.; Kino, G.; Moerner, W. Improving the Mismatch between Light and Nanoscale Objects with Gold Bowtie Nanoantennas. *Phys. Rev. Lett.* **2005**, *94*, 017402.

(7) Grigorenko, A.; Roberts, N.; Dickinson, M.; Zhang, Y. Nanometric Optical Tweezers Based on Nanostructured Substrates. *Nat. Photonics* **2008**, *2*, 365−370.

(8) Kollmann, H.; Piao, X.; Esmann, M.; Becker, S. F.; Hou, D.; Huynh, C.; Kautschor, L.-O.; Bösker, G.; Vieker, H.; Beyer, A.; et al. Toward Plasmonics with Nanometer Precision: Nonlinear Optics of Helium-Ion Milled Gold Nanoantennas. *Nano Lett.* **2014**, *14*, 4778−4784.

DOI: 10.1021/acsami.7b11428
ACS Appl. Mater. Interfaces 2017, 9, 36199−36205

(9) Yang, A.; Huntington, M. D.; Cardinal, M. F.; Masango, S. S.; Van Duyne, R. P.; Odom, T. W. Hetero-Oligomer Nanoparticle Arrays for Plasmon-Enhanced Hydrogen Sensing. *ACS Nano* **2014**, *8*, 7639−7647.
(10) Asbahi, M.; Mehraeen, S.; Wang, F.; Yakovlev, N.; Chong, K. S.; Cao, J.; Tan, M. C.; Yang, J. K. Large Area Directed Self-Assembly of Sub-10 Nm Particles with Single Particle Positioning Resolution. *Nano Lett.* **2015**, *15*, 6066−6070.
(11) Chen, Y. Q.; Bi, K. X.; Wang, Q. J.; Zheng, M. J.; Liu, Q.; Han, Y. X.; Yang, J. B.; Chang, S. L.; Zhang, G. H.; Duan, H. G. Rapid Focused Ion Beam Milling Based Fabrication of Plasmonic Nanoparticles and Assemblies Via "Sketch and Peel" Strategy. *ACS Nano* **2016**, *10*, 11228−11236.
(12) Koh, A. L.; Bao, K.; Khan, I.; Smith, W. E.; Kothleitner, G.; Nordlander, P.; Maier, S. A.; McComb, D. W. Electron Energy-Loss Spectroscopy(Eels) of Surface Plasmons in Single Silver Nanoparticles and Dimers: Influence of Beam Damage and Mapping of Dark Modes. *ACS Nano* **2009**, *3*, 3015−3022.
(13) Chu, M.-W.; Myroshnychenko, V.; Chen, C. H.; Deng, J.-P.; Mou, C.-Y.; Garcia de Abajo, F. J. Probing Bright and Dark Surface-Plasmon Modes in Individual and Coupled Noble Metal Nanoparticles Using an Electron Beam. *Nano Lett.* **2009**, *9*, 399−404.
(14) Duan, H.; Fernández-Domínguez, A. I.; Bosman, M.; Maier, S. A.; Yang, J. K. Nanoplasmonics: Classical Down to the Nanometer Scale. *Nano Lett.* **2012**, *12*, 1683−1689.
(15) Wiener, A.; Duan, H.; Bosman, M.; Horsfield, A. P.; Pendry, J. B.; Yang, J. K.; Maier, S. A.; Fernandez-Dominguez, A. I. Electron-Energy Loss Study of Nonlocal Effects in Connected Plasmonic Nanoprisms. *ACS Nano* **2013**, *7*, 6287−6296.
(16) Scholl, J. A.; Garcia-Etxarri, A.; Koh, A. L.; Dionne, J. A. Observation of Quantum Tunneling between Two Plasmonic Nanoparticles. *Nano Lett.* **2013**, *13*, 564−569.
(17) Lassiter, J. B.; Aizpurua, J.; Hernandez, L. I.; Brandl, D. W.; Romero, I.; Lal, S.; Hafner, J. H.; Nordlander, P.; Halas, N. J. Close Encounters between Two Nanoshells. *Nano Lett.* **2008**, *8*, 1212−1218.
(18) Yang, S.-C.; Kobori, H.; He, C.-L.; Lin, M.-H.; Chen, H.-Y.; Li, C.; Kanehara, M.; Teranishi, T.; Gwo, S. Plasmon Hybridization in Individual Gold Nanocrystal Dimers: Direct Observation of Bright and Dark Modes. *Nano Lett.* **2010**, *10*, 632−637.
(19) Brown, L. V.; Sobhani, H.; Lassiter, J. B.; Nordlander, P.; Halas, N. J. Heterodimers: Plasmonic Properties of Mismatched Nanoparticle Pairs. *ACS Nano* **2010**, *4*, 819−832.
(20) Yang, L.; Wang, H.; Fang, Y.; Li, Z. Polarization State of Light Scattered from Quantum Plasmonic Dimer Antennas. *ACS Nano* **2016**, *10*, 1580−1588.
(21) Li, G.-C.; Zhang, Y.-L.; Lei, D. Y. Hybrid Plasmonic Gap Modes in Metal Film-Coupled Dimers and Their Physical Origins Revealed by Polarization Resolved Dark Field Spectroscopy. *Nanoscale* **2016**, *8*, 7119−7126.
(22) Talley, C. E.; Jackson, J. B.; Oubre, C.; Grady, N. K.; Hollars, C. W.; Lane, S. M.; Huser, T. R.; Nordlander, P.; Halas, N. J. Surface-Enhanced Raman Scattering from Individual Au Nanoparticles and Nanoparticle Dimer Substrates. *Nano Lett.* **2005**, *5*, 1569−1574.
(23) Wustholz, K. L.; Henry, A.-I.; McMahon, J. M.; Freeman, R. G.; Valley, N.; Piotti, M. E.; Natan, M. J.; Schatz, G. C.; Van Duyne, R. P. Structure-Activity Relationships in Gold Nanoparticle Dimers and Trimers for Surface-Enhanced Raman Spectroscopy. *J. Am. Chem. Soc.* **2010**, *132*, 10903−10910.
(24) Simoncelli, S.; Roller, E. M.; Urban, P.; Schreiber, R.; Turberfield, A. J.; Liedl, T.; Lohmuller, T. Quantitative Single-Molecule Surface Enhanced Raman Scattering by Optothermal Tuning of DNA Origami-Assembled Plasmonic Nanoantennas. *ACS Nano* **2016**, *10*, 9809−9815.
(25) Farahani, J. N.; Pohl, D. W.; Eisler, H.-J.; Hecht, B. Single Quantum Dot Coupled to a Scanning Optical Antenna: A Tunable Superemitter. *Phys. Rev. Lett.* **2005**, *95*, 017402.
(26) Kinkhabwala, A.; Yu, Z.; Fan, S.; Avlasevich, Y.; Müllen, K.; Moerner, W. Large Single-Molecule Fluorescence Enhancements Produced by a Bowtie Nanoantenna. *Nat. Photonics* **2009**, *3*, 654−657.
(27) Acuna, G.; Möller, F.; Holzmeister, P.; Beater, S.; Lalkens, B.; Tinnefeld, P. Fluorescence Enhancement at Docking Sites of DNA-Directed Self-Assembled Nanoantennas. *Science* **2012**, *338*, 506−510.
(28) Li, G.-C.; Zhang, Y.-L.; Jiang, J.; Luo, Y.; Lei, D. Y. Metal-Substrate-Mediated Plasmon Hybridization in a Nanoparticle Dimer for Photoluminescence Line-Width Shrinking and Intensity Enhancement. *ACS Nano* **2017**, *11*, 3067−3080.
(29) Aouani, H.; Rahmani, M.; Navarro-Cia, M.; Maier, S. A. Third-Harmonic-Upconversion Enhancement from a Single Semiconductor Nanoparticle Coupled to a Plasmonic Antenna. *Nat. Nanotechnol.* **2014**, *9*, 290−294.
(30) Biswas, S.; Liu, X.; Jarrett, J. W.; Brown, D.; Pustovit, V.; Urbas, A.; Knappenberger, K. L., Jr.; Nealey, P. F.; Vaia, R. A. Nonlinear Chiro-Optical Amplification by Plasmonic Nanolens Arrays Formed Via Directed Assembly of Gold Nanoparticles. *Nano Lett.* **2015**, *15*, 1836−1842.
(31) Sönnichsen, C.; Reinhard, B. M.; Liphardt, J.; Alivisatos, A. P. A Molecular Ruler Based on Plasmon Coupling of Single Gold and Silver Nanoparticles. *Nat. Biotechnol.* **2005**, *23*, 741−745.
(32) Jain, P. K.; Huang, W.; El-Sayed, M. A. On the Universal Scaling Behavior of the Distance Decay of Plasmon Coupling in Metal Nanoparticle Pairs: A Plasmon Ruler Equation. *Nano Lett.* **2007**, *7*, 2080−2088.
(33) Teperik, T. V.; Nordlander, P.; Aizpurua, J.; Borisov, A. G. Robust Subnanometric Plasmon Ruler by Rescaling of the Nonlocal Optical Response. *Phys. Rev. Lett.* **2013**, *110*, 263901.
(34) Byers, C. P.; Hoener, B. S.; Chang, W. S.; Link, S.; Landes, C. F. Single-Particle Plasmon Voltammetry(Sppv) for Detecting Anion Adsorption. *Nano Lett.* **2016**, *16*, 2314−2321.
(35) Chen, J. I. L.; Chen, Y.; Ginger, D. S. Plasmonic Nanoparticle Dimers for Optical Sensing of DNA in Complex Media. *J. Am. Chem. Soc.* **2010**, *132*, 9600−9601.
(36) Shegai, T.; Johansson, P.; Langhammer, C.; Kall, M. Directional Scattering and Hydrogen Sensing by Bimetallic Pd-Au Nanoantennas. *Nano Lett.* **2012**, *12*, 2464−2469.
(37) Syrenova, S.; Wadell, C.; Langhammer, C. Shrinking-Hole Colloidal Lithography: Self-Aligned Nanofabrication of Complex Plasmonic Nanoantennas. *Nano Lett.* **2014**, *14*, 2655−2663.
(38) Lee, K.; Cui, Y.; Lee, L. P.; Irudayaraj, J. Quantitative Imaging of Single Mrna Splice Variants in Living Cells. *Nat. Nanotechnol.* **2014**, *9*, 474−480.
(39) Zhang, S.; Xu, H. Tunable Dark Plasmons in a Metallic Nanocube Dimer: Toward Ultimate Sensitivity Nanoplasmonic Sensors. *Nanoscale* **2016**, *8*, 13722−13729.
(40) Rycenga, M.; Xia, X.; Moran, C. H.; Zhou, F.; Qin, D.; Li, Z.-Y.; Xia, Y. Generation of Hot Spots with Silver Nanocubes for Single-Molecule Detection by Surface-Enhanced Raman Scattering. *Angew. Chem., Int. Ed.* **2011**, *50*, 5473−5477.
(41) Li, P.; Li, Y.; Zhou, Z. K.; Tang, S.; Yu, X. F.; Xiao, S.; Wu, Z.; Xiao, Q.; Zhao, Y.; Wang, H.; Chu, P. K. Evaporative Self-Assembly of Gold Nanorods into Macroscopic 3d Plasmonic Superlattice Arrays. *Adv. Mater.* **2016**, *28*, 2511−2517.
(42) Yang, S.; Dai, X.; Stogin, B. B.; Wong, T.-S. Ultrasensitive Surface-Enhanced Raman Scattering Detection in Common Fluids. *Proc. Natl. Acad. Sci. U. S. A.* **2016**, *113*, 268−273.
(43) Li, W.; Camargo, P. H. C.; Lu, X.; Xia, Y. Dimers of Silver Nanospheres: Facile Synthesis and Their Use as Hot Spots for Surface-Enhanced Raman Scattering. *Nano Lett.* **2009**, *9*, 485−490.
(44) Romero, I.; Aizpurua, J.; Bryant, G. W.; García De Abajo, F. J. Plasmons in Nearly Touching Metallic Nanoparticles: Singular Response in the Limit of Touching Dimers. *Opt. Express* **2006**, *14*, 9988−9999.
(45) Zuloaga, J.; Prodan, E.; Nordlander, P. Quantum Description of the Plasmon Resonances of a Nanoparticle Dimer. *Nano Lett.* **2009**, *9*, 887−891.
(46) Yu, X.; Lei, D. Y.; Amin, F.; Hartmann, R.; Acuna, G. P.; Guerrero-Martínez, A.; Maier, S. A.; Tinnefeld, P.; Carregal-Romero, S.; Parak, W. J. Distance Control in-between Plasmonic Nanoparticles Via Biological and Polymeric Spacers. *Nano Today* **2013**, *8*, 480−493.

DOI: 10.1021/acsami.7b11428
ACS Appl. Mater. Interfaces 2017, 9, 36199−36205

(47) Zhao, J.; Frank, B.; Burger, S.; Giessen, H. Large-Area High-Quality Plasmonic Oligomers Fabricated by Angle-Controlled Colloidal Nanolithography. *ACS Nano* **2011**, *5*, 9009−9016.
(48) Nemiroski, A.; Gonidec, M.; Fox, J. M.; Jean-Remy, P.; Turnage, E.; Whitesides, G. M. Engineering Shadows to Fabricate Optical Metasurfaces. *ACS Nano* **2014**, *8*, 11061−11070.
(49) Zhang, M.; Large, N.; Koh, A. L.; Cao, Y.; Manjavacas, A.; Sinclair, R.; Nordlander, P.; Wang, S. X. High-Density 2d Homo- and Hetero- Plasmonic Dimers with Universal Sub-10-Nm Gaps. *ACS Nano* **2015**, *9*, 9331−9339.
(50) Ogier, R.; Shao, L.; Svedendahl, M.; Kall, M. Continuous-Gradient Plasmonic Nanostructures Fabricated by Evaporation on a Partially Exposed Rotating Substrate. *Adv. Mater.* **2016**, *28*, 4658−4664.
(51) Masuda, H.; Fukuda, K. Ordered Metal Nanohole Arrays Made by a Two-Step Replication of Honeycomb Structures of Anodic Alumina. *Science* **1995**, *268*, 1466−1468.
(52) Jani, A. M. M.; Losic, D.; Voelcker, N. H. Nanoporous Anodic Aluminium Oxide: Advances in Surface Engineering and Emerging Applications. *Prog. Mater. Sci.* **2013**, *58*, 636−704.
(53) Lee, W.; Park, S.-J. Porous Anodic Aluminum Oxide: Anodization and Templated Synthesis of Functional Nanostructures. *Chem. Rev.* **2014**, *114*, 7487−7556.
(54) Wen, L.; Xu, R.; Mi, Y.; Lei, Y. Multiple Nanostructures Based on Anodized Aluminium Oxide Templates. *Nat. Nanotechnol.* **2017**, *12*, 244−250.
(55) Masuda, H.; Satoh, M. Fabrication of Gold Nanodot Array Using Anodic Porous Alumina as an Evaporation Mask. *Jpn. J. Appl. Phys.* **1996**, *35*, L126.
(56) Lei, Y.; Cai, W.; Wilde, G. Highly Ordered Nanostructures with Tunable Size, Shape and Properties: A New Way to Surface Nano-Patterning Using Ultra-Thin Alumina Masks. *Prog. Mater. Sci.* **2007**, *52*, 465−539.
(57) Lee, W.; Han, H.; Lotnyk, A.; Schubert, M. A.; Senz, S.; Alexe, M.; Hesse, D.; Baik, S.; Gösele, U. Individually Addressable Epitaxial Ferroelectric Nanocapacitor Arrays with near Tb Inch-2 Density. *Nat. Nanotechnol.* **2008**, *3*, 402−407.
(58) Dickey, M. D.; Weiss, E. A.; Smythe, E. J.; Chiechi, R. C.; Capasso, F.; Whitesides, G. M. Fabrication of Arrays of Metal and Metal Oxide Nanotubes by Shadow Evaporation. *ACS Nano* **2008**, *2*, 800−808.
(59) Wen, L.; Wang, Z.; Mi, Y.; Xu, R.; Yu, S. H.; Lei, Y. Designing Heterogeneous 1d Nanostructure Arrays Based on Aao Templates for Energy Applications. *Small* **2015**, *11*, 3408−3428.
(60) Hao, Q.; Huang, H.; Fan, X.; Hou, X.; Yin, Y.; Li, W.; Si, L.; Nan, H.; Wang, H.; Mei, Y.; et al. Facile Design of Ultra-Thin Anodic Aluminum Oxide Membranes for the Fabrication of Plasmonic Nanoarrays. *Nanotechnology* **2017**, *28*, 105301.
(61) Palik, E. D. *Handbook of Optical Constants of Solids*; Academic press: New York, 1998.
(62) Li, A.; Müller, F.; Birner, A.; Nielsch, K.; Gösele, U. Hexagonal Pore Arrays with a 50−420 Nm Interpore Distance Formed by Self-Organization in Anodic Alumina. *J. Appl. Phys.* **1998**, *84*, 6023−6026.
(63) Martín, J.; Manzano, C. V.; Caballero-Calero, O.; Martín-González, M. High-Aspect-Ratio and Highly Ordered 15-Nm Porous Alumina Templates. *ACS Appl. Mater. Interfaces* **2013**, *5*, 72−79.
(64) Sheikholeslami, S.; Jun, Y.-w.; Jain, P. K.; Alivisatos, A. P. Coupling of Optical Resonances in a Compositionally Asymmetric Plasmonic Nanoparticle Dimer. *Nano Lett.* **2010**, *10*, 2655−2660.
(65) Bachelier, G.; Russier-Antoine, I.; Benichou, E.; Jonin, C.; Del Fatti, N.; Vallee, F.; Brevet, P. F. Fano Profiles Induced by near-Field Coupling in Heterogeneous Dimers of Gold and Silver Nanoparticles. *Phys. Rev. Lett.* **2008**, *101*, 197401.
(66) Luk'yanchuk, B.; Zheludev, N. I.; Maier, S. A.; Halas, N. J.; Nordlander, P.; Giessen, H.; Chong, C. T. The Fano Resonance in Plasmonic Nanostructures and Metamaterials. *Nat. Mater.* **2010**, *9*, 707−715.
(67) Lombardi, A.; Grzelczak, M. P.; Pertreux, E.; Crut, A.; Maioli, P.; Pastoriza-Santos, I.; Liz-Marzan, L. M.; Vallee, F.; Del Fatti, N. Fano Interference in the Optical Absorption of an Individual Gold Silver Nanodimer. *Nano Lett.* **2016**, *16*, 6311−6316.

DOI: 10.1021/acsami.7b11428
ACS Appl. Mater. Interfaces 2017, 9, 36199−36205

Supporting Information

Controlled patterning of plasmonic dimers by using an ultra-thin nanoporous alumina membrane as a shadow mask

Qi Hao,[†,‡] Hao Huang,[‡,§] Xingce Fan,[§] Yin Yin,[†,∥] Jiawei Wang,[†] Wan Li,[‡] Teng, Qiu,[§] Libo Ma,[†,] Paul K. Chu[‡,*] and Oliver G. Schmidt[†,∥]*

[†] Institute for Integrative Nanosciences, Leibniz IFW Dresden, Helmholtzstraße 20, 01069 Dresden, Germany

[‡] Department of Physics and Materials Science, City University of Hong Kong, Tat Chee Avenue, Kowloon, Hong Kong, China

[§] Department of Physics, Southeast University, Nanjing 211189, P. R. China.

[∥] Material Systems for Nanoelectronics, Chemnitz University of Technology, Reichenhainer Str. 70, 09107 Chemnitz, Germany

*E-mail: l.ma@ifw-dresden.de (L. M.)

*E-mail: paul.chu@cityu.edu.hk (P. K. C.)

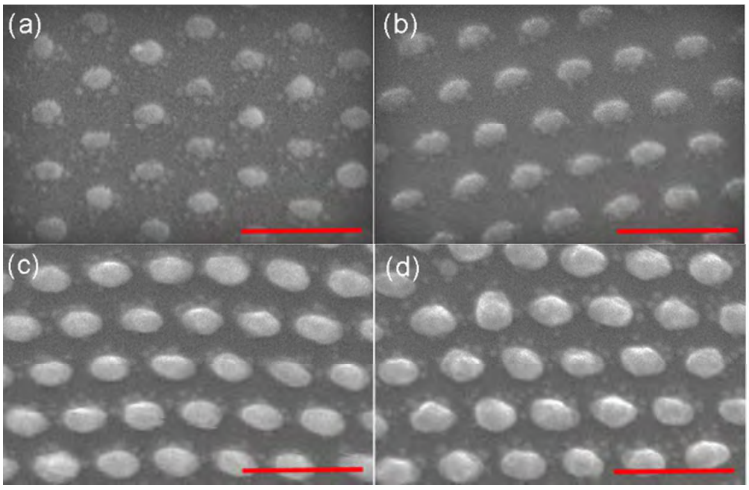

Figure S1. (a-d) SEM images of the fabricated single nanoparticle nanoarrays with different size of D = 31 nm (a), 35 nm (b), 42 nm (c) and 46 nm (d) by adopting different deposition angles of tan α = 9/45, 8/45, 7/45 and 6/45, respectively. We define the diameter of a spherical particle or the minor axis of an ellipsoidal particle as the particle size scale, D. The scale bars are 200 nm.

Table S1. Variations in the particle size scale (*D*) corresponding to the deposition angle *α*.

tan α / *D*(nm) / Pore diameter(nm)	5/45	6/45	7/45	8/45	9/45	10/45	11/45
70	42	37	31	26	20	n/A	n/A
75	47	42	36	31	25	19	n/A
80	52	47	41	36	30	24	19

*The data are obtained by calculating the aspect ratio (film thickness to pore diameter) of the AAO membrane and deposition angle. The film thickness is 250 nm.

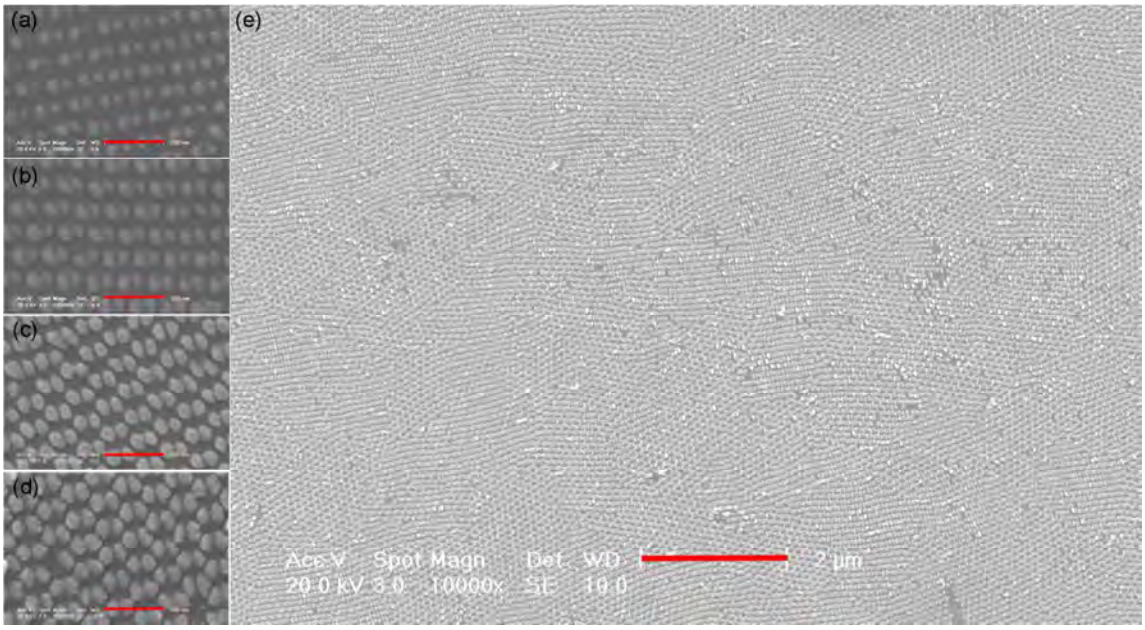

Figure S2. (a-d) SEM images of the plasmonic dimers with different particle size by adjusting the AAO pore diameter in shadow deposition; (e) Large-area SEM image of the plasmonic dimer array shown in (d). The scale bars in (a-d) is 200 nm and that in (e) is 2 μm.

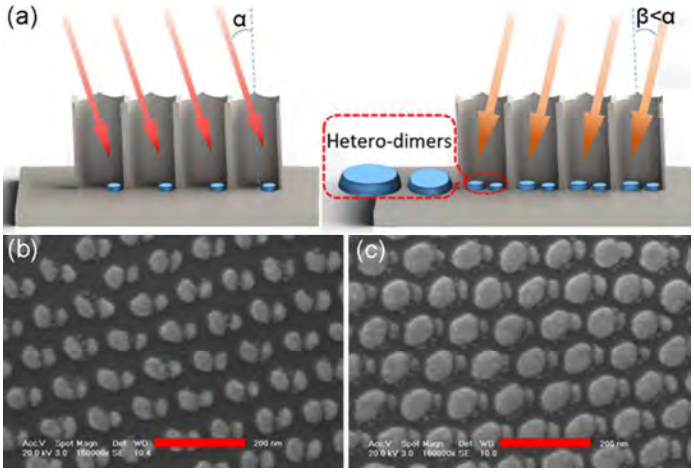

Figure S3. (a) Schematic showing the fabrication of the hetero-dimers with the deposition angles, α and β, individually controlled to adjust the particle size ratio; (b, c) SEM images of the hetero-dimers with particle size ratios of 3:2 and 3:1 by adopting different AAO membranes with pore diameters of 75 nm and 80 nm as well as different deposition angles of tan α = 9/45, tan β = 7/45 and tan α = 11/45, tan β = 5/45, respectively.

Appendix:

The enhancement factor (EF) of plasmonic dimers was determined by computing the ratio of SERS to normal Raman scattering (NRS) using the following expression:

$$\mathrm{EF} = \frac{I_{\mathrm{SERS}}/N_{\mathrm{SERS}}}{I_0/N_0} \quad (1)$$

where I_{SERS} and I_0 correspond to the integrated SERS and normal Raman scattering intensities, respectively. N_{SERS} and N_0 are the number of molecules probed in the SERS and normal Raman scattering measurements. Here we assume a 100% absorption for N_{sers} so the calculated EF is a lower-bound estimate. N_0 is determined by calculating the molecule concentration multiply by the laser probe volume.